

# **Advanced High Turning Compressor Airfoils for Low Reynolds Number Condition, Part 1: Design and Optimization**

**Toyotaka Sonoda, Yoshihiro Yamaguchi, Toshiyuki Arima, Markus Olhofer, Bernhard Sendhoff, Heinz-Adolf Schreiber**

**2003**

**Preprint:**

This is an accepted article published in Proceedings of the ASME Turbo Expo. The final authenticated version is available online at: [https://doi.org/\[DOI not available\]](https://doi.org/[DOI not available])

**GT2003-38458**

**ADVANCED HIGH TURNING COMPRESSOR AIRFOILS FOR LOW REYNOLDS  
NUMBER CONDITION  
PART1: DESIGN AND OPTIMIZATION**

**Toyotaka Sonoda Yoshihiro Yamaguchi Toshiyuki Arima**  
Honda R&D Co. Ltd., Wako Research Center  
Saitama 351-0193, Japan

**Markus Olhofer Bernhard Sendhoff**  
Honda Research Institute Europe GmbH  
63073 Offenbach, Germany

**Heinz-Adolf Schreiber**  
German Aerospace Center (DLR)  
Institute of Propulsion Technology  
D-51170 Köln, Germany

**ABSTRACT**

A high performance compressor airfoil at a low Reynolds number condition ( $Re=1.3\times 10^5$ ) has been developed using evolutionary algorithms in order to improve the performance of the outlet guide vane (OGV), used in a single low pressure turbine (LPT) of a small turbofan engine for business jet aircrafts. Two different numerical optimization methods, the Evolution Strategy (ES) and the Multi-Objective Genetic Algorithm (MOGA), were adopted for the design process to minimize the total pressure loss and the deviation angle at the design point at low Reynolds number condition. Especially, with respect to the MOGA, robustness against changes of the incidence angle is considered. The optimization process includes the representation of the blade geometry, the generation of a numerical grid and a blade-to-blade analysis using a quasi-three-dimensional (Q3D) Navier-Stokes solver with a  $k-\omega$  turbulence model including a newly implemented transition model to evaluate the performance. Overall aerodynamic performance and boundary layer properties for the two optimized blades are discussed numerically. The superior performance of the two optimized airfoils is demonstrated by a comparison with conventional controlled diffusion airfoils (CDA). The advantage in performance has been confirmed by detailed experimental investigations, which are presented in Part 2 of this paper.

**INTRODUCTION**

One approach to minimize the weight of small turbofan engines for business jet aircrafts is to design a single stage low-pressure turbine together with an outlet guide vane: the OGV is set just downstream of the single stage turbine in order to remove swirl. This way we hope to combine high efficiency at the cruise design point with the condition of a lightweight design.

The OGV had to be designed for high subsonic inlet speed, a high flow turning and a very low Reynolds number of about  $1.3\times 10^5$  at the cruise point. Although there are several publications on cascades at low Reynolds numbers, hardly any investigations have been reported on the detailed blade design for such high-turning, low Reynolds number compressor blades. Almost all of the papers deal with low speed cascades or with high speed cascades but low turning airfoils. Rhoden [1] reported that for very low speed cascades with a large camber angle a fairly high suction peak near the leading edge of the suction surface seems to be effective to prevent a laminar separation. However, questions remain whether this concept is valid for high inlet speed regions. Furthermore, additional analysis is required to determine the important factors for boundary layer transition and for laminar separation bubbles for very low Reynolds numbers (e. g. [2]). The initial design of the high turning guide vane section, first carried out

for ground condition ( $Re = 0.86 \times 10^6$ ), was based on the concept of a Controlled Diffusion Airfoil. A mid-span cross section of the 3D outlet guide vane and the design parameters are shown in Fig. 1 and Table 1, respectively. The design inlet Mach number is 0.60 and the design turning angle is 43 degrees. Because there is no streamtube contraction, the diffusion factor of 0.53 is relatively high. This blade is designated the baseline blade OGV-BASE.

In order to evaluate the performance of the baseline compressor blade experimentally, cascade tests have been carried out at DLR, Cologne [3] in a wide range of Reynolds numbers. The first results on the baseline cascade are given in Fig. 2, which shows the Reynolds number characteristics at two different incidence angles. It can be seen that for both cases the critical Reynolds number is about  $2 \times 10^5$  and that the losses dramatically increase below this number. Therefore, it is very important to understand the corresponding flow mechanism first and in a second step to develop a new design concept for an improved blade element in this critical regime.

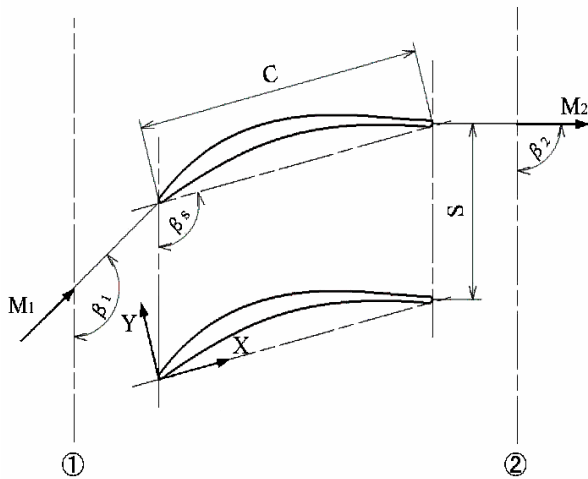


Fig. 1 Cascade parameters

Table 1 Design parameters of OGV-BASE

Aerodynamics		Geometry	
Inlet Mach Number, $M_1$	0.60	Stagger Angle, $\beta_s$	$104.6^\circ$
Inlet flow Angle, $\beta_1$	$133.0^\circ$	Chord Length (mm), C	65.0
Exit Flow Angle, $\beta_2$	$90.0^\circ$	Maximum Thickness	6.70%
Turning Angle, $\beta_1 - \beta_2$	$43.0^\circ$	Solidity, C/S	1.734
Diffusion Factor, DF	0.53		
AVDR	1.0	Reynolds number	$8.7 \times 10^5$

Recently, first results on the optimization of compressor airfoils have been reported [4, 5]. The complete design method consists of a geometrical representation of the airfoil, a blade-to-blade flow solver and a numerical optimization algorithm. Koeller et al. [4] used a combination of stochastic and gradient algorithms for the optimization, and a third-order spline for the representation. Benini and Toffolo [5] used an evolutionary algorithm that belongs to the class of global stochastic optimization methods together with a Bezier spline. Both approaches used a viscous/inviscid solver (MISES [6]) for the blade-to-blade analysis. In both studies the Reynolds number was quite high (in the order of  $2.5 \times 10^6$ ) which leads to a relatively simple flow field compared to the present condition ( $Re = 1.3 \times 10^5$ ). Since in our project phenomena like large laminar separation bubbles and intensive turbulent separations are likely to play a dominant role, it seems inevitable to use a Navier-Stokes solver for the evaluation.

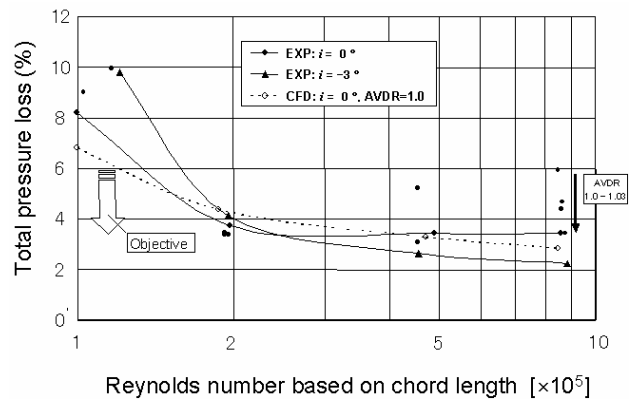


Fig.2 Experimental and calculated Reynolds number characteristics of baseline CDA cascade

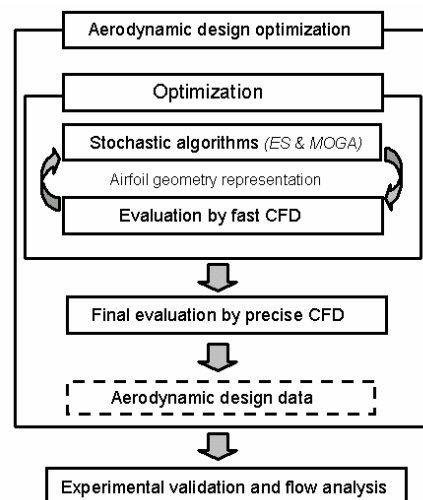


Fig.3. Design approach for the high turning compressor airfoil for low Reynolds numbers

As shown in Fig. 3, two different methods belonging to the class of evolutionary algorithms, the Evolution Strategy (ES) and the Multi-Objective Genetic Algorithm (MOGA) have been employed for the optimization. We used a Navier-Stokes solver first during the optimization in a “fast” mode and later for validation before the experiments were executed in a “precise” mode. In the precise mode a new transition model adapted to the low Reynolds number regime with a fine mesh resolution in the boundary layer is used. Such a fine resolution is omitted in the fast mode in order to save computation time taking into account that during the optimization the flow solver will be called 6000 (ES) and 12000 (MOGA) times, repeating. The final designs were experimentally validated at DLR, Cologne and additional flow analysis was carried out to support the interpretation of the experimental results.

It is well known that free-stream turbulence occurring in real turbomachinery environments has a strong effect on the boundary layer; it tends to cause early transition from laminar to turbulent flow [7] and it may alter the separation behavior. However, in the present work the free-stream turbulence level for the optimization process has been set to the low turbulent level of 0.6% that is similar to the one in the planned experiments to allow a thorough and reasonable verification of the design.

In Part 1 of the two contributions the focus has been put on the results of the aerodynamic design optimization and in Part 2 on the validation and the flow analysis. Here the target was to elucidate why the optimized airfoils have a superior performance.

**Validation of fast Navier-Stokes solver.** As the fast flow solver, an in-house quasi-three-dimensional (Q3D) version of the Navier-Stokes flow solver, HSTAR (Honda Software for Turbomachinery Aerodynamics Research) with a low Reynolds  $k-\epsilon$  turbulence model proposed by Chien [8] is used. The Q3D flow solver is a modified 3D Navier-Stokes code [9] for the purpose of calculating aerodynamical performance of 2D cascades in short time. The grid consists of  $191 \times 51$  cells and the average value of  $y^+$  near the wall is of the order of 1.0. The computation time for one run with this grid is about 3.5 minutes on an HP Alpha 21264 833MHz processor. In the optimization process, AVDR has been always fixed to 1.0.

A typical example for the validation of the fast flow solver (no transition model) is shown in Fig. 2. The CFD results do not clearly show a sudden increase below the critical Reynolds number as it is observed in the experiment. However, qualitatively the overall Reynolds number characteristics are well predicted. Figure 4 shows a blade surface Mach number distribution of the Reynolds number of  $2 \times 10^5$  for two incidence angles. At design incidence ( $\beta_1 = 133^\circ$ ), the experimental Mach number distribution on the suction surface shows a laminar separation from about 30 to 55% of chord. A more extended bubble is obtained at the negative incidence ( $\beta_1 = 130^\circ$ ). Both lead to a certain amount of additional drag and

performance deterioration. It is interesting to note that the  $k-\epsilon$  model without an explicit transition model is able to simulate a similar mid-chord separation and provides a reasonable loss level. Therefore, it seems acceptable that this fast approach is applied during the optimization process.

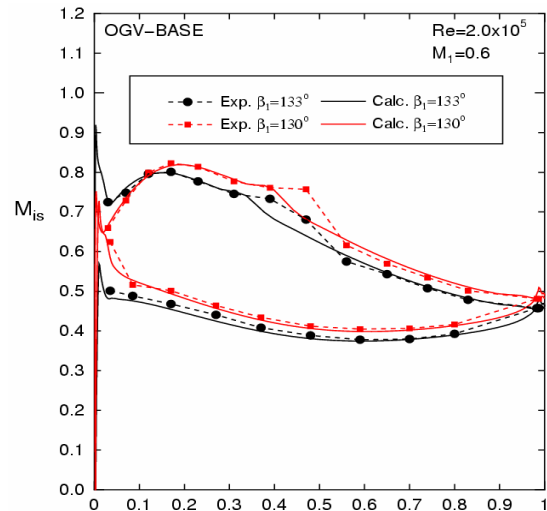


Fig. 4 Comparison of experiment and CFD simulation (no transition model) in profile Mach number distribution

## NOMENCLATURE

AVDR	axial velocity density ratio: $AVDR = (\rho_2 u_2) / (\rho_1 u_1)$
$c$	chord length
$C_f$	skin friction coefficient $= \tau_w / (0.5 \rho_1 u_1^2)$
$H_{12}$	shape factor $= \delta_1 / \delta_2$
$i$	incidence angle
$k$	turbulent kinetic energy
$M$	Mach number
$p$	pressure
$r$	radius
$Re$	Reynolds number based on chord length
$s$	blade spacing
$Tu$	free-stream turbulence level, in %
$u$	velocity
$x$	chordwise coordinate
$y^+$	dimensionless distance from wall
$\beta$	flow angle with respect to cascade front
$\gamma$	stagger angle
$\delta_1$	boundary layer displacement thickness
$\delta_2$	boundary layer momentum thickness
$\delta\beta$	tolerance for exit flow angle
$\mu$	dynamic viscosity
$\mu_T$	turbulent viscosity
$\rho$	density
$\tau_w$	wall shear stress
$\theta$	blade metal angle

- $\omega$  total pressure loss coefficient:  $\omega = (p_{t1} - p_t)/(p_{t1} - p_1)$ , or specific dissipation of turbulent kinetic energy
- $\Theta_{\min}$  minimum thickness of blade
- $\Theta_{\max}$  maximum thickness of blade

**Additional nomenclature for the optimization**

- $b_1$  minor axis of leading edge ellipse
- $b_2$  minor axis of trailing edge ellipse
- PS(i) control points on pressure surface
- SS(i) control points on suction surface
- $W_1$  wedge-in angle
- $W_2$  wedge-out angle
- $r_{L12}$  ratio of minor to major axis of leading edge ellipse
- $r_{T12}$  ratio of minor to major axis of trailing edge ellipse

**Subscripts**

- 1 inlet plane upstream of leading edge
- 2 exit plane downstream of trailing edge
- is isentropic entity
- LE leading edge
- TE trailing edge
- t total

**DESIGN APPROACH**

**Evolutionary Algorithms for Design Optimization**

Evolutionary algorithms belong to the class of global stochastic optimization algorithms. They are based on principles of evolutionary biology, in particular on natural selection acting on a population of different designs called

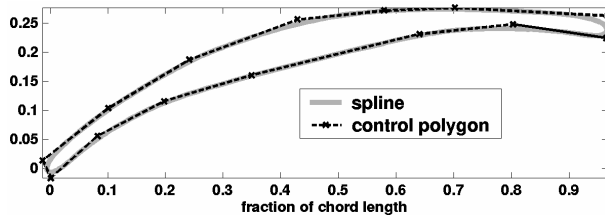


Fig 5 Airfoil parameterization of ES

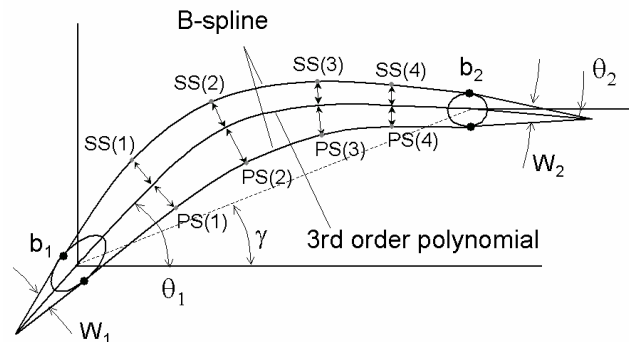


Fig. 7 Airfoil parameterization of MOGA

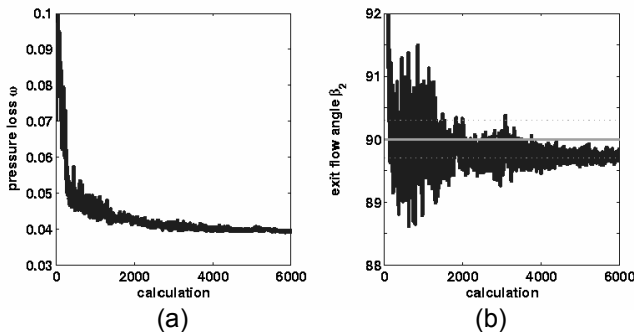


Fig. 6 Fitness values during optimization, (a) total pressure loss, (b) exit flow angle

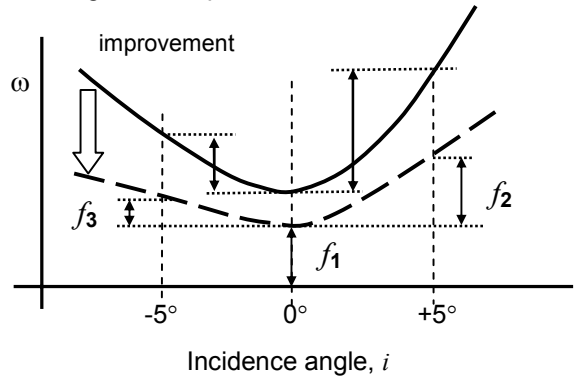


Fig. 8 Goal of optimization process of MOGA

individuals. The variation operators produce genetic diversity and the selection directs the evolutionary search. Recombination or crossover which combines genetic material and mutation which introduces stochastic changes, are the main variation operators.

In this paper, we employ two algorithms that represent two different approaches to the search process with respect to the representation, to the variation operators and in particular to the design of the fitness function. The CMA-ES, which was employed in the design of the OGV-ES blade, is a single-objective algorithm and belongs to the evolution strategies. The MOGA, which was employed in the design of the OGV-MOGA blade, belongs to the class of Pareto-based multi-objective algorithms [10, 11] and its evolutionary principles are based on the genetic algorithm.

For both optimizations, the inlet flow angle, the real chord length and the solidity are fixed by design requirements. In order to analyze a wide variety of possible design concepts, the geometrical constraints were not the same for the CMA-ES and the MOGA method. This has the drawback that the results cannot be directly compared from an optimization point of view.

## Optimization with ES

In the design of the ES blade, a special variant of evolution strategies with so-called co-variance matrix adaptation (CMA) has been applied. The details of the CMA-ES are quite involved and the reader is referred to Hansen et al. [12] for the implementation used here and to Olhofer et al. [13] for the application of the CMA-ES to design optimization problems.

**Blade profile definition.** A closed non-uniform third order rational B-spline [14] is used for the representation of the blade, as shown in Figure 5. The control points are subject to the optimization and the resulting spline determines the contour of the represented blade. In this optimization, the parameter vector consists of 14 spline control points, where each control point is represented by three coordinates. Therefore, in total there are 42 parameters that are optimized. This allows a high degree of freedom for variations during the optimization. Nevertheless, the number of parameters is small enough to allow a convergence of the algorithm within a reasonable number of generations.

**Objective function.** In order to calculate the fitness, three different criteria have to be considered: the pressure loss of the design, the deviation angle and the thickness of the blade. In principle, two different approaches are possible to cope with multiple criteria for the evaluation of the quality of the design: a weighted sum approach or a Pareto-based approach. In the design of the ES blade we employed the weighted sum approach as follows:

$$f = \sum_{i=1}^6 w_i t_i \rightarrow \text{minimize}, \quad (1)$$

where the  $w_i$  are weighting coefficients, which are fixed heuristically, and the  $t_i$  are given as follows:

$$\begin{aligned} t_1 &= \max(0, |\beta_2 - \beta_{2,design}| - \delta\beta) \\ t_2 &= \omega \\ t_3 &= \max(0, r_{LE,design} - r_{LE}) \\ t_4 &= \max(0, r_{TE,design} - r_{TE}) \\ t_5 &= \max(0, \Theta_{min,design} - \Theta_{min}) \\ t_6 &= \max(0, \Theta_{max,design} - \Theta_{max}) \end{aligned} \quad (2)$$

**Constraints.** The tolerance of the exit flow angle  $\delta\beta$  is set to  $0.3^\circ$ . The values of  $r_{TE,design}$ ,  $r_{LE,design}$ ,  $\Theta_{max,design}$ , and  $\Theta_{min,design}$  are lower limits. The first three are set identical to those of the BASE airfoil, and the last is set to  $0.9 \times 2 \times \text{radius}$  of the trailing edge of OGV-BASE. No explicit criterion for the off-design incidence conditions is considered.

**Convergence of the ES-CMA.** In Figure 6, the development of the pressure loss and the exit flow angle are shown. A  $(\mu, \lambda)$  CMA-ES with one parent-individual ( $\mu=1$ ) and  $\lambda=12$  offspring-individuals in each generation was used. The optimization was initialized with a geometry similar to the BASE airfoil in the first generation. A fast decrease of the pressure loss as well as a rapid adaptation of the deviation angle can be observed. Later on the deviation angle fluctuates near the target angle of 0.3 degree, whereas the pressure loss is further decreased. The resulting airfoil of this optimization is shown in Fig.15 together with the MOGA and BASE airfoils.

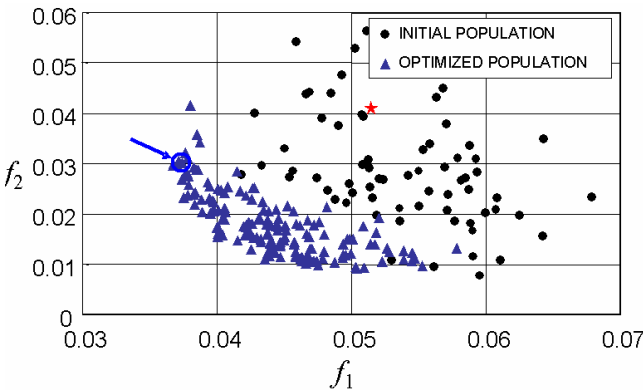


Fig. 9 Pareto distribution of the initial population and the optimized population projected on  $f_1$  vs.  $f_2$  plane

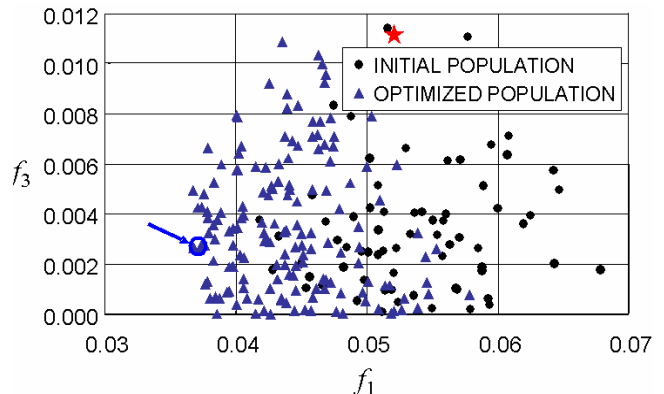


Fig. 10 Pareto distribution of the initial population and the optimized population projected on  $f_1$  vs.  $f_3$  plane

## Optimization with MOGA

The basic algorithm of the MOGA is the same as the simple real-valued genetic algorithm. However, as the name suggests the MOGA approach incorporates extensions to allow a multi-objective search process with the target to approximate the Pareto surface, see [10, 11], by the population of the final generation. A blade that belongs to the Pareto set is a non-dominated solution, i.e., no other blade geometry exists which is superior in *all* objectives. Therefore, MOGAs can generate a set of Pareto solutions that demonstrate trade-off relationships between the objective functions. These relationships can improve the decision-making process of the aerodynamic engineer and provide useful information for a design-parameter study. MOGAs have been successfully applied to the aerodynamic optimization of gas-turbine blades, see e.g. work by Yamaguchi et al. [15] and Oyama et al. [16].

**Blade profile definition.** The blade surface is described with a B-spline [14] using four control points based on a *preliminary-camber* line. Note that the *preliminary-camber* line is different from the mean camber-line, since the control points on the suction surface and the pressure surface are defined independently in the optimization process. Furthermore, two points are used to describe the leading edge ellipse and the trailing edge ellipse for the pressure surface and the suction surface, respectively. Figure 7 shows a profile of the design parameterization.

**Objective functions.** In this study, in addition to the performance at design condition, the off-design performance is considered as schematically shown in Fig. 8. The corresponding objective functions are defined as follows:

1. Minimization of the pressure loss coefficient at design incidence

$$f_1 = \omega \rightarrow \text{minimize} \quad (3)$$

2. Wide operating range for positive incidence

$$f_2 = \left| \omega_{\text{design}} - \omega_{\text{design}+5^\circ} \right| \rightarrow \text{minimize} \quad (4)$$

3. Wide operating range for negative incidence

$$f_3 = \left| \omega_{\text{design}} - \omega_{\text{design}-5^\circ} \right| \rightarrow \text{minimize} \quad (5)$$

**Constraints.** The tolerance of the outflow angle  $|\beta_2 - \beta_{2,\text{design}}|$  is set to  $\pm 1^\circ$ . Furthermore, the lower bounds of  $\Theta_{\min}$ ,  $b_1$  and  $b_2$  are given by  $\Theta_{\min, \text{design}} = 0.9 \times 2 \times (\text{radius of the trailing edge})$  and by  $r_{LE, \text{design}}$  and  $r_{TE, \text{design}}$ :

$$\Theta_{\min} > \Theta_{\min, \text{design}}; \quad b_1 > r_{LE, \text{design}}; \quad b_2 > r_{TE, \text{design}} \quad (6)$$

**Convergence in MOGA.** In this optimization, the target is to obtain all Pareto solutions in a three dimensional space of objectives. In order to visualize the 2D Pareto surface more clearly, we projected two objectives onto one in Figures 9 and 10 resulting in two 2D Pareto distributions. Figure 9 shows the distribution of individuals at the initial generation and the final generation on the  $f_1$  vs.  $f_2$  objective plane. Figure 10 shows the corresponding distributions for the  $f_1$  vs.  $f_3$  plane. From the individuals in the final generation in Figs. 9 and 10, one blade geometry highlighted by an arrow was selected as the MOGA airfoil, therefore, putting emphasis on the performance at design condition. For comparison, the baseline airfoil is represented by stars in Figs. 9 and 10.

A summary of the essential features of both optimization methods (ES and MOGA) is given in Table 2.

Table 2 Summary of two global stochastic optimization methods used

Algorithm		( $\mu, \lambda$ )-CMA-ES	MOGA
Design parameters		42 (=14 of control points x 3)	14
Representation		NURBS (cyclic, 3rd order)	B-spline (3rd order)
Constraints	Thickness	$r_{LE} > 0.8\% \times c$ $r_{TE} > 1.1\% \times c$ $\Theta_{\min} > 2.0\% \times c$ $\Theta_{\max} > 6.7\% \times c$	$b_1 > 0.8\% \times c$ $b_2 > 1.1\% \times c$ $\Theta_{\min} > 2.0\% \times c$ $\Theta_{\max} \rightarrow \text{no constraint}$
	Exit deviation angle	$-0.3^\circ > \beta_2 > +0.3^\circ$	$-1.0^\circ > \beta_2 > +1.0^\circ$
Objective function		Single objective (Eq. 1) weighted sum of 1. exit deviation angle constraint 2. pressure loss 3. four thickness constraints	Three objectives (Eqs. 3, 4, 5) $f_1 = \text{pressure loss}$ $f_2 = \text{difference of pressure losses (i=0^\circ, +5^\circ)}$ $f_3 = \text{difference pressure losses (i=0^\circ, -5^\circ)}$
Population size		$\mu = 1, \lambda = 12$	80
Number of generations		500	50
Total number of NS-calls		6000 (=500x12)	12000 (=80x50x3)
Initial blade		OGV-BASE	Uniform distributed

## Validation of precise flow solver

As the precise flow solver, a  $k-\omega$  turbulence model [17] and an Abu-Ghannam/Shaw (AGS) transition model [18], based on Drela's modification [6], which has been successfully used in the MISES code, are implemented into the quasi-three-dimensional version of HSTAR [9].

**Transition model.** Transition starts when the momentum thickness Reynolds number  $Re_{\delta_2}$  exceeds a critical transition Reynolds number  $Re_{tr}$ , and it is completed when  $Re_{\delta_2}=2Re_{tr}$ . The critical transition Reynolds number is calculated from the following relation used by Kuegler [19], that is based on the modification by Drela [6] to remove the ill-posedness of the original AGS model:

$$Re_{tr} = 163 + 74.3 \left[ 0.55 + \tanh \left( \frac{10}{H_{12}} - 5.5 \right) + 1 \right] \cdot (0.94 \cdot n_{cr} + 1), \quad (7)$$

where,  $H_{12} = \delta_1 / \delta_2$ . The influence of the free-stream turbulence outside of the boundary layer  $Tu$  is given by the critical amplification factor  $n_{cr}$ :

$$n_{cr} = -8.43 - 2.4 \ln \left( \frac{Tu}{100} \right). \quad (8)$$

Outside the boundary layer the flow is assumed to be turbulent. The combination of the transition and the turbulence model is realized by introducing an intermittency function  $f_t$  to modify the turbulent viscosity  $\mu_T$  obtained from the turbulence model, as follows:

$$\mu_T = f_t \frac{\rho k}{\omega}, \quad (9)$$

where

$$f_t = \left[ 25 / \left[ 25 + 275 \left\{ 1 - \sin \left( \frac{\pi}{2} \cdot \frac{Re_{\delta_2} - Re_{tr}}{Re_{tr}} \right) \right\} \right] \right]^3. \quad (10)$$

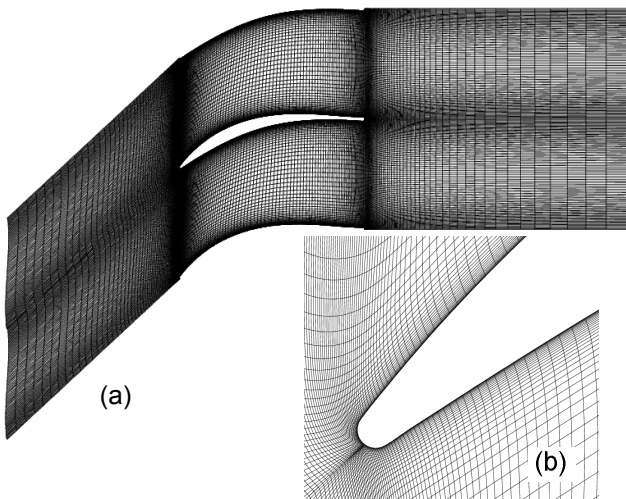


Fig. 11 Computational grid, (a) overall, (b) leading edge part in detail

**Validation.** For the validation, the experimental data for the baseline cascade were used again. The computational grids are shown in Fig. 11. The grid consists of  $251 \times 81$  cells, which is therefore finer than the one used in the fast mode ( $191 \times 51$ ). The average  $y^+$  of the first grid point from the wall is about 0.3 for calculations at  $Re \approx 2.0 \times 10^5$ . The comparison between computed results and experimental data is shown in Fig. 12. In Fig. 12 (a) the isentropic Mach number distributions obtained at  $Re=1.97 \times 10^5$ ,  $M_1=0.60$ , and  $\beta_1=130^\circ$  are shown for the fully turbulent ( $k-\omega$  and Chien's  $k-\epsilon$  model) and transitional analysis ( $k-\omega$  plus transition model) in comparison to the measured data. The measurement data show a nearly constant Mach number in the region of laminar separation between about 30% to 47% of the chord and a transition region with turbulent re-attachment and a large pressure recovery from about 45% to 57% of chord. In the computed results, this phenomenon can be predicted with the  $k-\omega$  turbulence model and the transition model only.

A further validation is provided in Fig. 12 (b), that shows a comparison between simulated and experimental Reynolds number characteristics for  $\beta_1=133^\circ$  and  $M_1=0.6$ . Compared to the case without the transition model, see Fig. 2, the prediction accuracy is considerably improved. As a last validation, a computed incidence characteristic for the subcritical conditions with high losses ( $Re=1.0 \times 10^5$ ) is shown in Fig. 12 (c). Although the experimental losses scatter around slightly high values ( $\beta_1=133^\circ$ ), the computed curve is qualitatively similar to the experimental one.

The computed flow field with the transitional analysis is shown in Fig. 13, again at  $Re=1.97 \times 10^5$ , and  $\beta_1=130^\circ$ . The computed skin friction coefficient with the isentropic Mach number along the suction surface is shown in Fig. 13 (a), the eddy viscosity contour in Fig. 13 (b), and the velocity vector with the static pressure contour in Fig. 13 (c). From Fig. 13 (a) we notice that the laminar separation starts around 30% of chord on the blade suction surface. The augmentation of the eddy viscosity starts at approximately 45% chord, a position that corresponds to the Mach number or pressure kink in the suction side distribution. Downstream of the pressure kink the negative skin friction coefficient is amplified due to the high vorticity of the reverse flow and the turbulent entrainment process along the rear part of the bubble. Turbulent re-attachment is simulated around 57% of chord, where the eddy viscosity increases. These observations agree well with the explanation of a separated-flow transition discussed e.g. in the 1991 IGTI scholar lecture of Mayle [20] and the pattern of the computed skin friction coefficient is similar to the one shown by Walker [21].

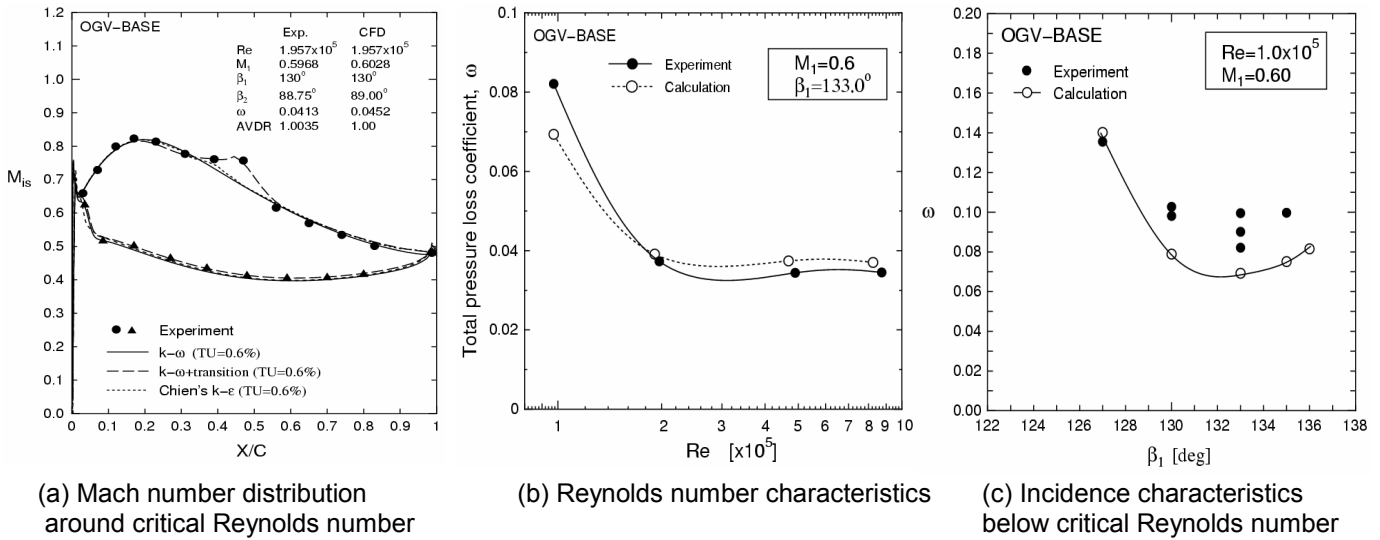


Fig. 12 Comparison of experimental and CFD results for OGV-BASE. In CFD, the  $k-\omega$  model with transition model was applied.

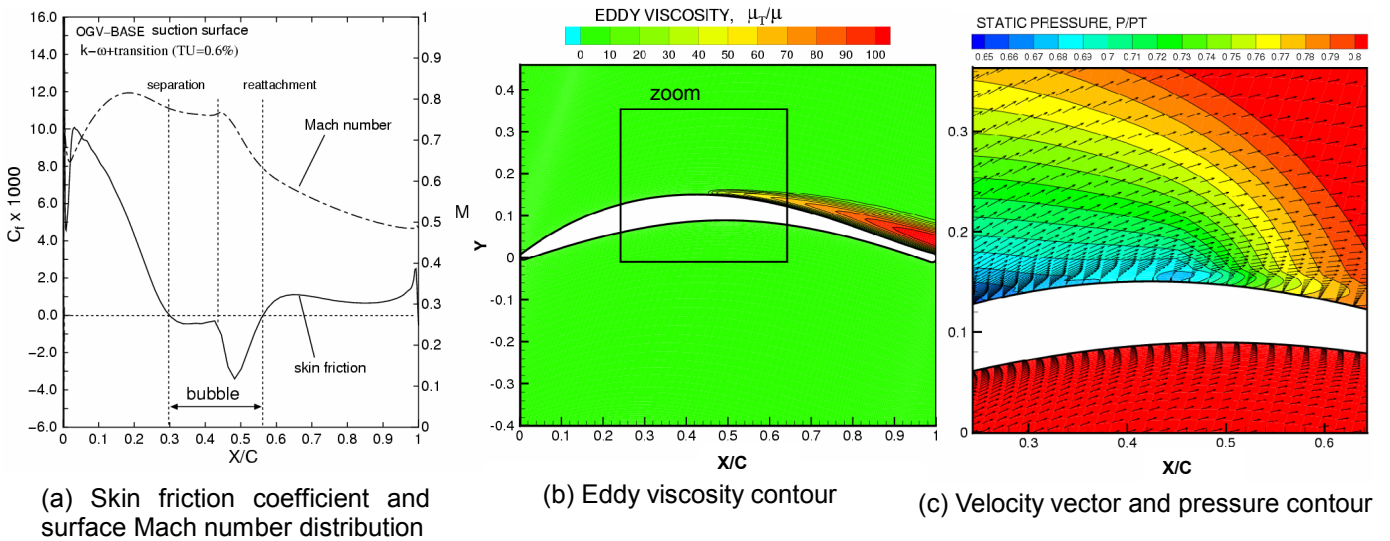


Fig. 13 Computed results with a  $k-\omega$  turbulence and transition model at  $Re \approx 2 \times 10^5$ ,  $\beta_1 = 130^\circ$

### Reynolds number effect on boundary layer of OGV-BASE

To analyze the effect of the Reynolds number in more detail, in Fig 14, the computed blade Mach number distributions (top), the simulated boundary thickness parameters and form factor (middle), and the suction surface friction coefficient (bottom) are provided for Reynolds numbers of 1.0, 2.0 and  $8.7 \times 10^5$ . As shown in Fig. 12 (b), the losses above a Reynolds number of  $2.0 \times 10^5$  remain nearly constant, whereas for smaller

Reynolds numbers a rapid increase can be observed. Since the computed Mach number distributions agree quite well with the experimental data, the computed boundary layer data and skin friction coefficient seem to be plausible.

For a high Reynolds number of  $Re = 8.7 \times 10^5$  (including  $4.9 \times 10^6$ , not shown here), the boundary layer transition occurs near the blade leading edge and flow remains turbulent all along the surface. However, the boundary layer thickens and the skin friction coefficient decreases while moving toward the

blade trailing edge. In reality, the boundary layer tends to separate from the rear part of the suction surface.

At the Reynolds number of  $2.0 \times 10^5$ , a laminar separation bubble with transition and turbulent re-attachment is observed between 25% and 48% of chord. The boundary layer thickness indicates that the laminar separation is less pronounced, and the bubble has little impact on the loss level. However, at

lower Reynolds number ( $Re=1.0 \times 10^5$ ), an extended laminar separation is observed with a tendency not to re-attach on the surface, see Fig. 14 (right). This critical situation is often interpreted as “bubble burst” associated with a considerable loss increase. The present simulation predicts a loss of 6.9%.

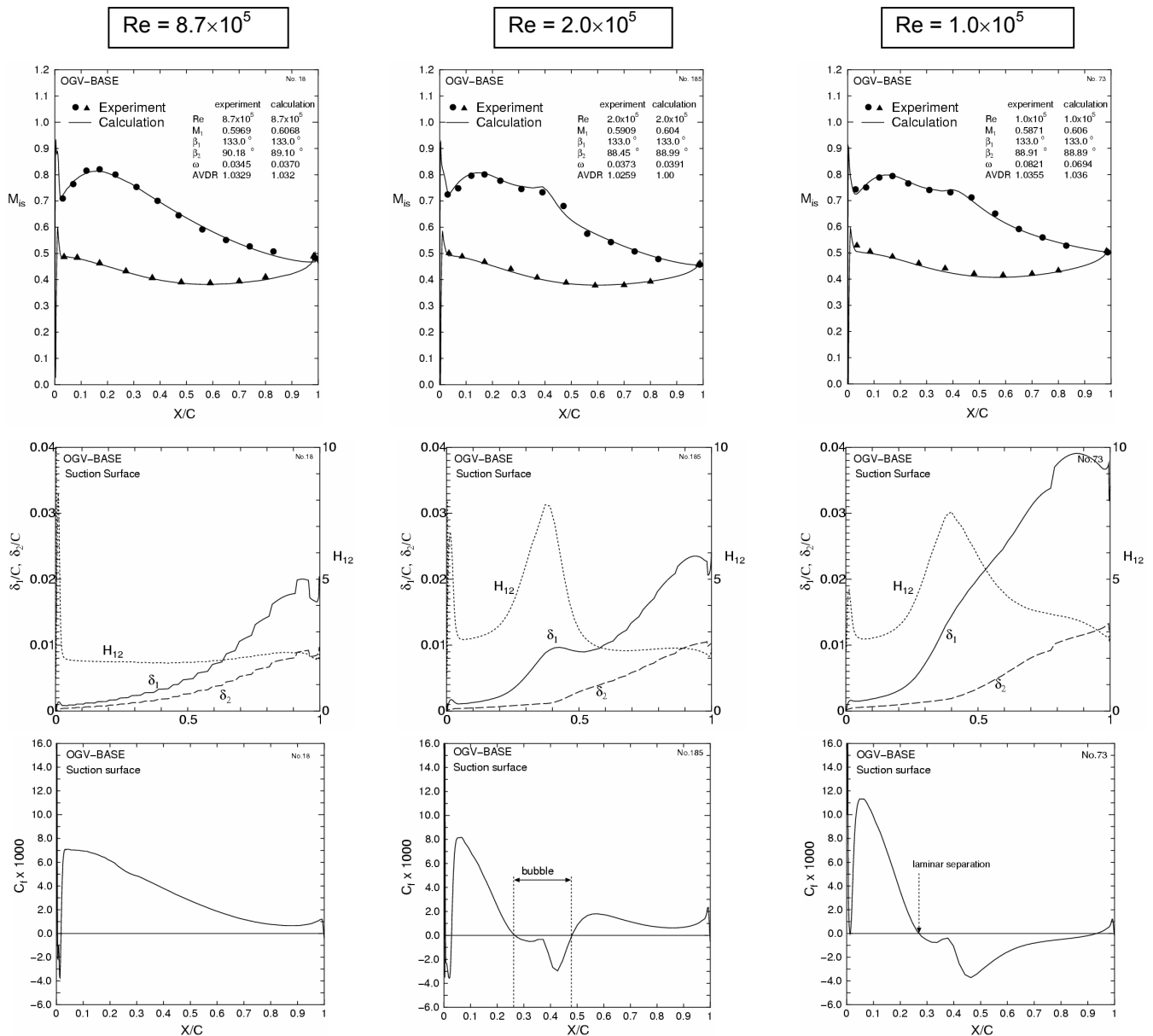


Fig. 14 Effect of Reynolds number on suction side boundary layer property for OGV-BASE. Surface isentropic Mach number (top), boundary layer property (middle), and skin friction coefficient (bottom), k- $\omega$  turbulence- and transition model applied

## OPTIMIZATION RESULTS

### Airfoils Geometry

The airfoil geometry resulting from the two optimization methods ES and MOGA are shown together with the baseline profile in Fig. 15. Figures 15 (a), (b) and (c) show all blade geometries with fixed LE points, the details of the LE parts and the chord-wise suction surface curvature variations between 10% and 50% of the chord, respectively. Unique airfoil geometries have been obtained, having maximum thickness at around mid-chord (ES) and more in the rear part of the chord for the MOGA airfoil. The stagger angles of the two optimized blades are also significantly different. Furthermore, the LE thickness of the MOGA profile is decreased, as shown in Fig. 15 (b). The LE geometries of OGV-BASE, OGV-MOGA and OGV-ES are circular, elliptic and "arbitrary". The present aerodynamic simulations show that the LE and suction side flow fields seem to be significantly controlled by the resulting variations of the suction-surface curvature of the optimized blades, as shown in Fig. 15 (c). For the OGV-ES, the first local minimum of the curvature is located at about 15% chord, whereas for OGV-MOGA it is at 40% of chord.

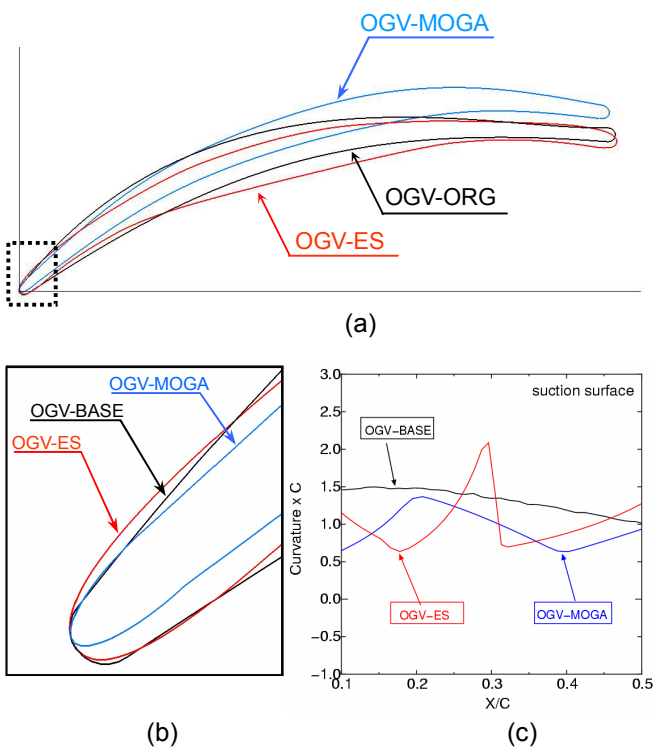


Fig. 15 Two optimized airfoils compared to baseline geometry, (a) blade profile, (b) leading edge part in detail, (c) curvature of suction surface

### Overall Aerodynamic Characteristics

**Reynolds number characteristics.** As a main result, the computed loss vs. Reynolds number characteristics for the two optimized airfoils ES and MOGA are shown in Fig. 16 for the design incidence ( $AVDR = 1.0$ ) and compared to previous results of the baseline airfoil. The white circles for OGV-BASE are taken from Fig. 12 (b) in which the  $AVDR$  was slightly adjusted to the experiments. Therefore, the losses of OGV-BASE have been recalculated at the design Reynolds number with  $AVDR=1.0$  and plotted as double circles.

The numerical results clearly demonstrate that both optimized blades are superior in the whole Reynolds number range and that a dramatic loss reduction was achieved at the design point with  $Re = 1.3 \times 10^5$ . There is no sign of a steep increase of the total pressure losses below a certain critical Reynolds number in the tested range. Another interesting point is that there seems to be a minimum loss point around  $Re=1.8 \times 10^5$  for the MOGA airfoil; refer to part 2 for a detailed discussion.

**Incidence angle characteristics.** A computed incidence angle characteristics for the optimized airfoils and for the baseline profile is shown in Fig. 17 for the design Reynolds number of  $1.3 \times 10^5$  and  $AVDR=1.0$ . Again the performance of OGV-BASE at the design Reynolds number with  $AVDR=1.0$  is recalculated and plotted as double circles. The incidence range is fairly increased both for the negative as well as for the positive incidence range. Especially, the OGV-MOGA results show lower losses between  $134^\circ$  and  $137^\circ$  compared to OGV-ES but slightly higher ones at very negative incidences.

An explanation for these differences can be obtained from the blade surface Mach number distribution at the design incidence angle of  $133.0^\circ$ : As shown in Fig. 18 (top) the Mach number distribution is very different between the OGV-ES and MOGA profile. One reason why two different types of loading patterns have been obtained is the difference between the constraints for the ES and the MOGA optimization. In the case of OGV-ES, which was optimized for the design incidence only, the Mach number distribution shows an extreme front loading type, while the maximum LE peak Mach number of OGV-MOGA is slightly decreased to achieve lower losses at the high incidences. As a result of the simulations Fig. 17 clearly reflects that OGV-MOGA with a smaller peak Mach number shows superior performance on the positive incidence side and OGV-ES seems to be marginally better at the very negative incidences.

It is interesting to note that the optimized blades show a similar performance around the design flow angle of  $133.0^\circ$ , although both airfoil geometries are very different from each other. The Mach number distribution of the OGV-ES has an extreme forward located suction side Mach number maximum – a distribution similar to the one found in the low speed C4-cascade tests of Rhoden [1] with minimum losses. Here, earlier boundary layer transition from laminar to turbulent flow seems

to be important for low Reynolds numbers, and the well controlled front loading airfoil leads to a good performance.

### Boundary Layer Characteristics at Design Reynolds number

Figure 18 shows the computed isentropic profile Mach number distributions (top), the computed boundary layer property on the suction surface (middle), and the skin friction coefficient (bottom) for OGV-BASE, OGV-ES and OGV-MOGA, respectively, for the design Reynolds number of  $1.3 \times 10^5$ . In Table 3 the corresponding aerodynamic parameters for the three cascades are summarized. For OGV-BASE, a well developed laminar separation bubble is observed on the suction surface in Fig. 18 (left). The laminar separation occurs at around 25% of chord and extends to approximately 90% of chord; a situation at which a “bubble burst” associated with high losses ( $\omega = 0.06$ ) can be expected. For OGV-ES, an early laminar separation bubble and transition at around 21% of chord is observed due to the strong adverse pressure gradient right from the beginning (Fig. 18 center). Downstream of transition this gradient is continuously relaxed toward the TE to keep the boundary layer far apart from turbulent separation.

The computed result shows that the laminar separation starts around 7% of chord from leading edge. Turbulent re-attachment is observed at approximately 25% of chord. On the MOGA airfoil, a small LE separation bubble is observed (Fig. 18 right), however, transition is not completed. The flow re-laminarizes due to a weak re-acceleration at around 10% to 20% of chord and the boundary layer thickness remains thin, see  $\delta_1$  and  $\delta_2$  in Fig. 18 (right). Laminar separation finally occurs at around 31% to 50% of chord with turbulent re-attachment.

The bubble positions for the two optimized blades correspond to local curvature minima at positions of about 15% (OGV-ES) and about 40% (OGV-MOGA) as shown in Fig. 15 (c). On the other hand, the curvature for the baseline airfoil is monotonically decreased downstream but shows a higher level in the bubble position in relation to those of ES and MOGA. It seems that the boundary layer development is significantly controlled by the airfoil surface curvature underneath the bubble.

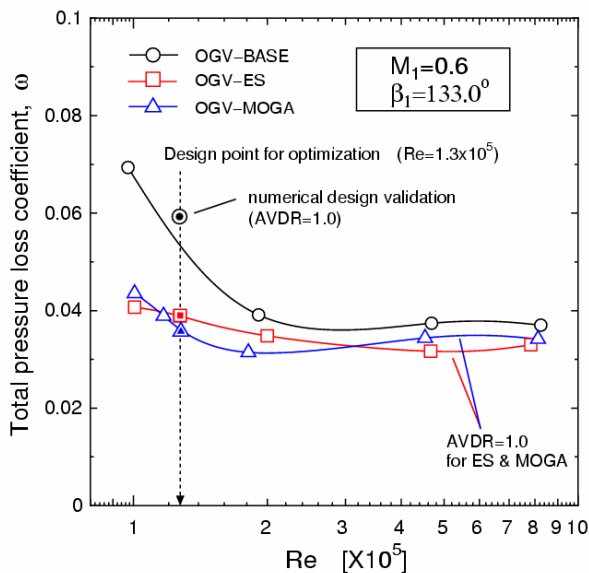


Fig. 16 Computed Reynolds number characteristics of three airfoils at design inlet flow angle of  $133^\circ$

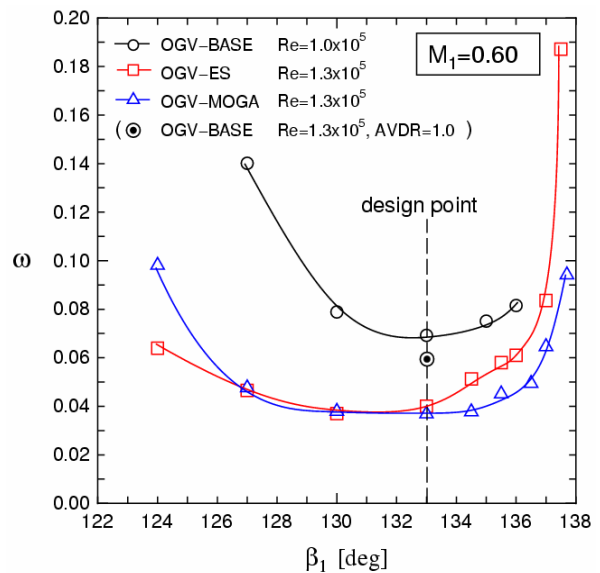


Fig. 17 Computed incidence characteristics of three airfoils at low Reynolds number of about  $1.2 \times 10^5$

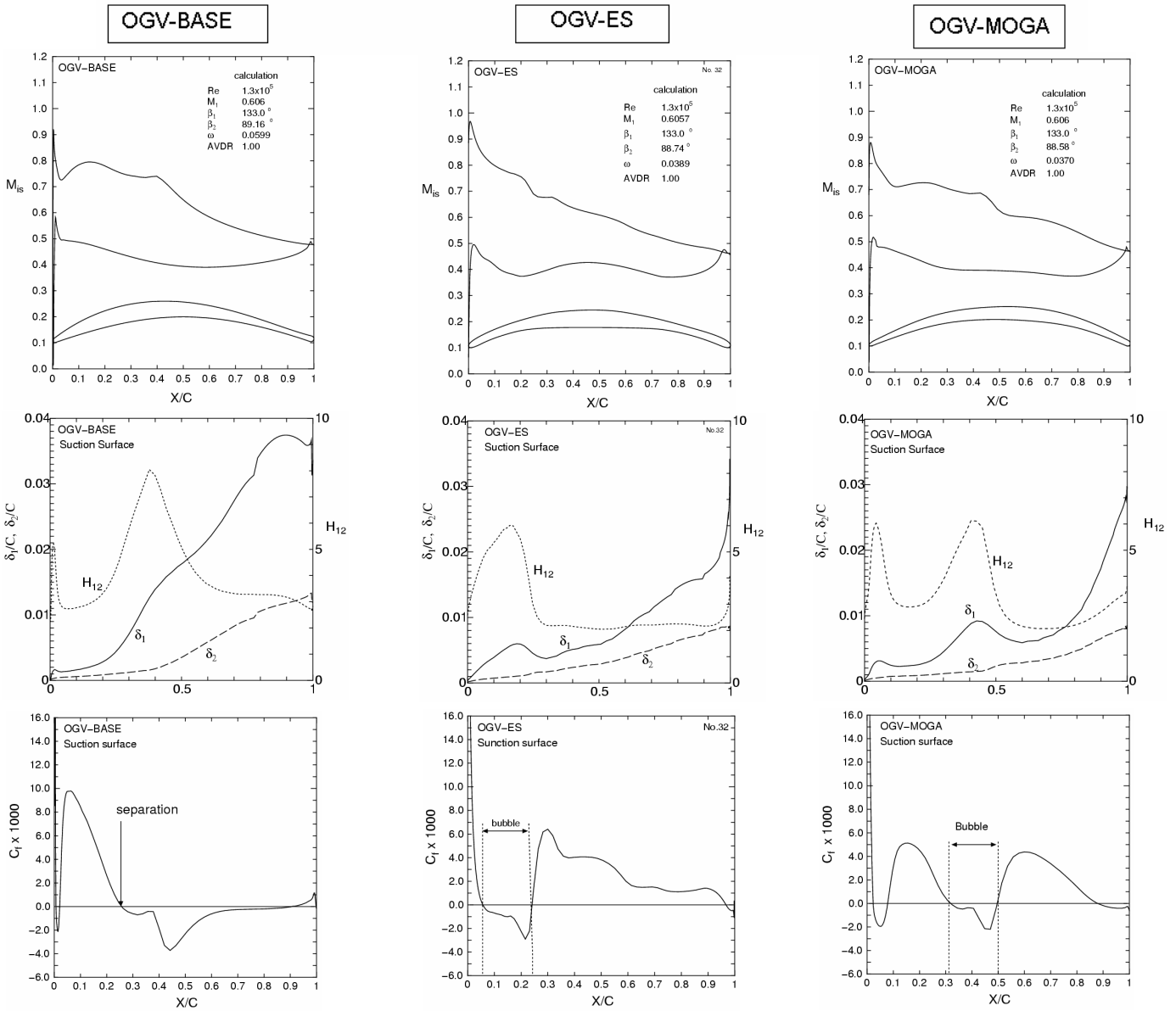


Fig. 18 Computed surface isentropic Mach number (top), boundary layer properties (middle), and skin friction coefficient (bottom) at design point ( $Re=1.3 \times 10^5$ ,  $M_1=0.6$ , and  $\beta_1=133^\circ$ ) for the baseline airfoil (OGV-BASE) and two optimized airfoils (OGV-ES and OGV-MOGA)

Table 3 Computed performance for two optimized airfoils and baseline airfoil at low Reynolds number

	$Re \times 10^{-5}$	$M_1$	$M_2$	$\beta_1$	$\beta_2$	$p_2/p_1$	AVDR	$\omega$
OGV-ES	1.3	0.606	0.397	$133^\circ$	$88.74^\circ$	1.134	1.0	0.0389
OGV-MOGA	1.3	0.606	0.398	$133^\circ$	$88.58^\circ$	1.136	1.0	0.0370
OGV-BASE	1.3	0.606	0.399	$133^\circ$	$89.16^\circ$	1.123	1.0	0.0599

## CONCLUSIONS

Evolutionary optimization methods, namely evolution strategy and the multi-objective genetic algorithm, have been applied to the design of a high turning compressor airfoil at very low Reynolds numbers together with a Navier-Stokes solver with Chien's low Reynolds  $k-\epsilon$  turbulence model. Furthermore, the aerodynamic characteristics and the boundary layer properties for the baseline blade OGV-BASE and the two optimized airfoils OGV-ES and OGV-MOGA have been numerically analyzed using a newly developed flow solver that combines a  $k-\omega$  turbulence model with an Abu-Ghannam/Shaw (AGS) transition model. The following conclusions can be drawn.

1. The results from the optimization algorithms without an explicit transition model in the flow solver show better performance for a wide range of Reynolds numbers in the numerical design validation than the baseline.
2. The superior performance of the optimized airfoils for very low Reynolds numbers is gained without losing performance at high Reynolds numbers.
3. The boundary layer analysis shows a large separation bubble for the baseline airfoil which is close to "bubble burst", but relatively smaller separation bubbles with less drag for the two optimized airfoils.
4. In the case of OGV-ES, which was optimized only at the design incidence angle, a well controlled front loading airfoil leads to an earlier boundary layer transition which in turn leads to a high performance for low Reynolds numbers.
5. The OGV-MOGA cascade, which was optimized at off-design incidences as well as design incidence, obtained a slightly reduced velocity maximum at the leading edge with moderate local pressure gradients and the suction side partly remained laminar until about mid chord.
6. The bubble positions for the optimized blades correspond to the positions with local curvature minima of the airfoil suction surface. Therefore, the curvature underneath the bubble seems to play an important role to minimize the bubble height and the associated drag and losses.

The experimental validation of the performance of the optimized airfoils and additional analysis are carried out in part 2 of this paper.

## ACKNOWLEDGEMENTS

The authors are grateful to Wolfgang Steinert, who performed the test series, to Anton Weber and Harald Greza (all from the Institute of Propulsion Technology, DLR) and to Yaochu Jin and Edgar Körner (both from Honda R&D Europe) for helpful discussions and useful comments on the CFD

simulation and the optimization. Finally, we thank Honda R&D Co., Ltd. for the permission to publish these results.

## REFERENCES

- [1] Rhoden, H.G., 1952, "Effects of Reynolds Number on the Flow of Air through a Cascade of Compressor Blades," ARC, R&M No. 2919.
- [2] Roberts, W.B., 1975, "The Effect of Reynolds Number and Laminar Separation on Axial Cascade Performance," *ASME Journal of Engineering for Power*, Vol. 97, pp. 261-274.
- [3] Schreiber, H.A., Steinert, W., Sonoda, T., and Arima, T., 2003, "Advanced High Turning Compressor Airfoils for Low Reynolds Number Condition, Part 2: Experimental and Numerical Analysis," ASME Paper GT-2003-38477.
- [4] Koeller, U., Moenig, R, Kuesters, B., and Schreiber, H.A., 2000, "Development of Advanced Compressor Airfoils for Heavy-Duty Gas Turbines, Part 1: Design and Optimization," *ASME Journal of Turbomachinery*, Vol. 122, pp. 397-405.
- [5] Benini, E., and Toffolo, A., 2002, "Development of High-Performance Airfoils for Axial Flow Compressor Using Evolutionary Computation," *AIAA Journal of Propulsion and Power*, Vol. 18, No. 3, pp. 544-554.
- [6] Drela, M., 1998, "MISES Implementation of Modified Abu-Ghannam/Shaw Transition Criterion (Second Revision)," MIT Aero-Astro.
- [7] Schreiber, H.A., Steinert, W., and Kuesters, B., "Effect of Reynolds Number and Free-Stream Turbulence on Boundary Layer Transition in a Compressor Cascade," *ASME Journal of Turbomachinery*, Vol. 124, pp. 1-9.
- [8] Chien, J. Y., 1982, "Predictions of Channel and Boundary Layers With a Low-Reynolds-Number Two Equation Model of Turbulence," *AIAA Journal*, Vol. 20, pp. 33-38.
- [9] Arima, T., Sonoda, T., Shirotori, M. Tamura, A., and Kikuchi, K., 1999, "A Numerical Investigation of Transonic Axial Compressor Rotor Flow Using a Low-Reynolds-Number  $k-\epsilon$  Turbulence Model," *ASME Journal of Turbomachinery*, Vol. 121, pp.44-58.
- [10] Goldberg, D. E., 1989, "Genetic Algorithms in Search, Optimization, and Machine Learning," Addison-Wesley, Reading, MA.
- [11] Fonseca, C. M., and Fleming, P. J., 1993, "Genetic Algorithms for Multiobjective Optimization: Formulation, Discussion, and Generalization," *Proceedings of the 5th International Conference on Genetic Algorithms*.
- [12] Hansen, N. and Ostermeier, A., 1996, "Complete Derandomized Self-adaptation in Evolution Strategies: The Covariance Matrix Adaptation," In *Proceedings 1996 IEEE International Conference on Evolutionary Computation*, pp. 312-317, IEEE Press.
- [13] Olhofer, M., Arima, T., Sonoda, T., Fischer, M. and Sendhoff, B., 2001, "Aerodynamic Shape Optimisation Using Evolution Strategies," In I.C. Parmee and P. Hajela (Eds.), *Optimisation in Industry*, pp. 83-94, Springer Verlag.

- [14] Piegl, L. and Tiller, W., 1997, "*The NURBS Book*," 2nd edition, Springer-Verlag.
- [15] Yamaguchi, Y., and Arima, T., 2002, "Aerodynamic Optimization for the Compressor Stator Blade," In I.C. Parmee and P. Hajela (Eds.), *Optimization in Industry*, pp.163-172, Springer Verlag.
- [16] Oyama, A., and Liou, M. S., 2002, "Multiobjective Optimization of a Multi-Stage Compressor using Evolutionary Algorithm," AIAA paper 2002-3545.
- [17] Wilcox, D. C., 1988, "Reassessment of the Scale-Determining Equation for Advanced Turbulence Models," *AIAA Journal*, Vol. 26, No. 11, pp.1299-1310.
- [18] Abu-Ghannam, B. J., and Shaw. R., 1980, "Natural Transition of Boundary Layers – The Effects of Turbulence, Pressure Gradient, and Flow History," *Journal of Mechanical Engineering Science*, Vol. 22, No. 5, pp.213-228.
- [19] Kuegeler, E, Weber, A., and Lisiewicz, S., 2001, "Combination of a Transition Model with a Two-Equation Turbulence Model and Comparison with Experimental Results," *The 4th European Turbomachinery Conference*, ATI-CST-076/01.
- [20] Mayle, R. E., 1991, "The Role of Laminar-Turbulent Transition in Gas Turbine Engines," *The 1991 IGTI scholar lecture*, *ASME Journal of Turbomachinery*, Vol. 113, pp.509-531.
- [21] Walker, G.J., 1993, "The Role of Laminar-Turbulent Transition in Gas Turbine Engines: A Discussion," *ASME Journal of Turbomachinery*, Vol. 115, pp. 207-217.